ACSNANO

www.acsnano.org

ARTICLE

Protein@Inorganic Nanodumpling System for High-Loading Protein Delivery with Activatable Fluorescence and Magnetic Resonance Bimodal Imaging Capabilities

Xiaohua Zhu, Rui Tang, Shigong Wang, Xiaoye Chen, Jiajun Hu, Chunyang Lei, Yan Huang, Honghui Wang, Zhou Nie,* and Shouzhuo Yao

Cite This: *ACS Nano* 2020, 14, 2172–2182

Read Online

ACCESS | Metrics & More | Article Recommendations | Supporting Information

ABSTRACT: **Efficient protein delivery into the target cell is highly desirable for protein therapeutics. Current approaches for protein delivery commonly suffer from low-loading protein capacity, poor specificity for target cells, and invisible protein release. Herein, we report a protein@inorganic nanodumpling (ND) system as an intracellular protein delivery platform. Similar to a traditional Chinese food, the dumpling, ND consists of a protein complex "filling" formed by metal-ion-directed self-assembly of protein cargos fused to histidine-rich green fluorescent proteins (H_{39}GFPs), which are further encapsulated by an external surface "wrapper" of manganese dioxide (MnO_2) *via in situ* biomineralization. This ND structure allows for a high loading capacity (>63 wt %) for protein cargos with enhanced stability. NDs can be targeted and internalized into cancer cells specifically through folic acid receptors by surface-tailored folic acid. The protein cargo release is in a bistimuli-responsive manner, triggered by an either reductive or acidic intracellular microenvironment. Moreover, the MnO_2 nanowrapper is an efficient fluorescence quencher for inner fused GFPs and also a "switch-on" magnetic resonance imaging (MRI) agent *via* triggered release of Mn^{2+} ions, which enables activatable fluorescence/MRI bimodal imaging of protein release. Finally, the ND is highly potent and specific to deliver functional protein ribonuclease A (RNase A) into cultured target cells and the tumor site in a xenografted mouse model, eliminating the tumor cells with high therapeutic efficacy. Our approach provides a promising alternative to advance protein-based cancer therapeutics.**

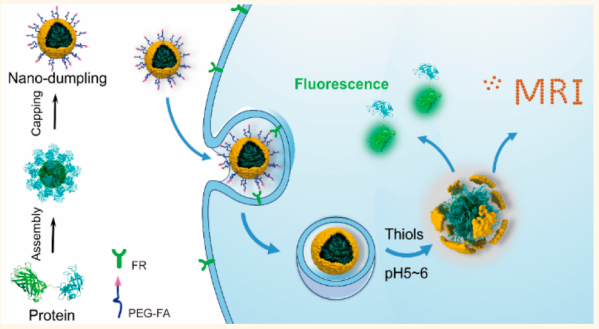

KEYWORDS: *protein delivery, biomineralization, protein encapsulation, activatable imaging, magnetic resonance imaging*

Therapeutic proteins are one of the fastest developing modalities of biologics medicine.[1,2] To date, more than 130 pharmacological proteins have been approved for clinical use.[3] Most approved protein drugs target cell-surface antigens and extracellular domains of receptors, such as monoclonal antibodies,[4] cytokines,[5] and growth factors.[6] Due to poor membrane permeability for proteins, efficient delivery of proteins to access intracellular targets remains a major challenge.[7,8] Hence, developing a strategy for intracellular protein delivery has emerged as a promising field for protein therapeutics.

In recent decades, the general strategy to deliver protein is to fuse the protein cargos with cell-membrane penetration tags, including protein transduction domains (PTDs),[9] transmembrane signals,[10] and supercharged proteins.[11,12] This method facilitates protein endocytosis, whereas it often suffers from nonspecific cellular internalization and low protein stability in the serum. Nanomaterial-based therapeutic carriers have recently been presented as promising alternative approaches to enable targeted protein delivery and spatiotemporally controlled release, including liposomes,[13,14] polymers,[15,16] nanogels,[17,18] and inorganic nanoparticles.[19,20] However, their applicability is potentially limited by low loading for protein therapeutics (<20% of protein by weight)[21] or complicated

Received: November 14, 2019
Accepted: January 28, 2020
Published: January 28, 2020

https://dx.doi.org/10.1021/acsnano.9b09024
ACS Nano 2020, 14, 2172–2182

fabrication processes under conditions unfavorable to protein activity (*e.g.*, organic solvents).[22] Moreover, most delivery carriers lack molecular imaging modalities, and *ex situ* identifications of protein cargos are normally required. Such processes are slow and unavailable for real-time evaluation on protein delivery efficacy *in vivo*. Thus, to overcome the above-mentioned issues, ideal protein carriers should show (1) controllable encapsulation with high protein loading; (2) simple "green" preparation preferable for protein activity; (3) excellent stability in biofluids; (4) targeted delivery to diseased cells/organs; and (5) visualization of protein release *via* real-time imaging.

In order to enable these ideal features in one single protein carrier, we show here the rational design of a "dumpling-like" protein@inorganic nanostructure for imaging-guided protein delivery *in vivo*. This nanocarrier, termed nanodumplings (NDs), is inspired by the dumpling, a traditional Chinese food with a core filling surrounded by a wrapper (Scheme 1A). We

Scheme 1. Illustration of ND-Facilitated Protein Delivery[a]

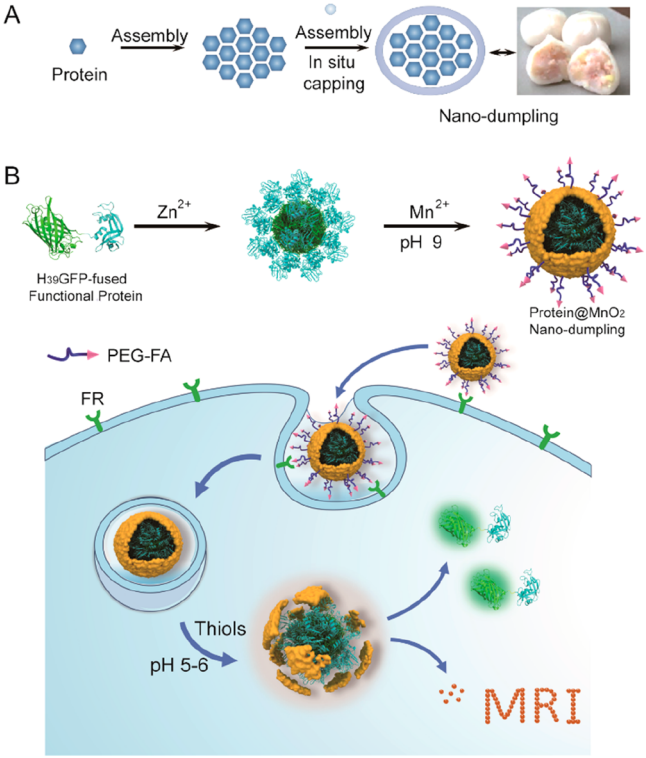

[a](A) Protein preassembly strategy to design a dumpling-like nanosystem for protein delivery. (B) Schematic illustration of efficient cancer cell targeting and fluorescence/MRI bimodal visualized intracellular protein delivery by NDs.

also take inspiration from the dumpling preparation process to design a "protein preassembly" strategy to fabricate the proposed NDs, in which protein cargos are preassembled to form a nanosized complex "filling" followed by *in situ* synthesis of an inorganic nanomaterial outer layer (wrapper). It is different from conventional nanocarrier preparation strategies of postsynthesis loading (protein loading after nanomaterials synthesis). As a proof-of-concept, a preassembled protein complex was formed by a metal-ion-directed self-assembly of protein cargo, which was fused to an assembling tag, a histidine-rich green fluorescent protein (H_{39}GFP). The protein complex is wrapped by a manganese dioxide (MnO_2) external surface "wrapper" *via in situ* biomineralization and further functionalized with folic-acid-modified polyethylene glycol (PEG-FA) for active targeting. The protein preassembly and protein@inorganic structure render NDs with not only a high protein loading capacity (>63 wt %), a simple "green" fabrication, and the excellent protection of the protein cargos but also specific cancer cell targeting, a stimuli-responsive release manner, and an activatable fluorescence/magnetic resonance imaging (MRI) bimodal imaging capability. The NDs couple the advantageous features of fusion-engineered protein carriers and nanomaterial-based delivery vehicles, presenting a highly efficient and smart self-reporting protein delivery carrier that could selectively and efficiently deliver functional proteins *in vivo* with real-time release tracking by fluorescence/MRI bimodal imaging.

ND fabrication starts with tag-mediated self-assembly *via* the histidine–Zn^{2+} interaction to form a protein H_{39}GFP/Zn^{2+} protein complex, followed by *in situ* biomineralization of the MnO_2 nanowrapper using outer interfaces of the H_{39}GFP/Zn^{2+} protein complex as a template. NDs are further functionalized with PEG-FA for active targeting to the folate receptor (FR)-overexpressed tumor cells (Scheme 1B). The MnO_2 nanowrapper offers a protective layer to inner protein cargos, and its redox and acid-sensitive properties allow bistimuli-responsive self-disassembly, triggered by the intracellular reductive and acidic microenvironment.[23,24] The extensive and broad light absorption capacity of MnO_2 nanomaterials enables them to quench the fluorescence of diverse fluorophores through energy transfer.[25] Therefore, the MnO_2 nanowrapper is an efficient fluorescence quencher of inner fused GFPs, and also a "turn-on" MRI contrast agent where released Mn^{2+} ions upon its disassembly allow contrast amplification.[26] Hence, the intact ND is quiescent for both fluorescence and MRI signals. As FR is highly expressed in target cancer cells, NDs can specifically recognize target cells and are internalized *via* the receptor-mediated endocytosis. After that, the acidic environment (pH 5–6) inside the endosome/lysosome and high concentration of intracellular thiols (glutathione, GSH, or cysteine, Cys) destroy the MnO_2 nanowrapper and disassemble the H_{39}GFP/Zn^{2+} complex. The reactions lead to the massive release of payloads with the H_{39}GFP tag, the fluorescence recovery lightening the protein release sites, and the production of a large amount of Mn^{2+} ions enabling the MRI detection. In comparison with conventional "stay-on" protein delivery fluorescence-tracking platforms using fluorophore labeling, the NDs provide dual-activatable fluorescence/MRI bimodal imaging functionalities, which allows imaging of the intracellular release process of proteins more precisely in a temporal and spacial manner. Moreover, the MRI mode of NDs is of significance for evaluation of protein delivery efficacy at the whole body level, which are not capable for current protein delivery carriers.

RESULTS AND DISCUSSION

Zn^{2+}-Directed Protein Assembly. The construction of NDs depends on the preassembly of proteins to form the H_{39}GFP/Zn^{2+} complex filling, which allows for high loading capacity for protein cargos. In order to enable protein cargos with self-assembly functionality, we fuse functional proteins with a self-assembly tag, H_{39}GFP. This GFP contains 39 histidine residues, among which 12 pairs of adjacent dihistidine motifs were on its surface (Figure S1). Such a dihistidine motif has been used for the assembly of protein/peptide superstructures due to its high chelation affinity with metal ions. We expected that the

https://dx.doi.org/10.1021/acsnano.9b09024
ACS Nano 2020, 14, 2172–2182

self-assembly of protein cargos could be induced by metal-ion-mediated interprotein coordination between H_{39}GFP tags (Figure 1A). The zinc ion (Zn^{2+}) is one of the most widely

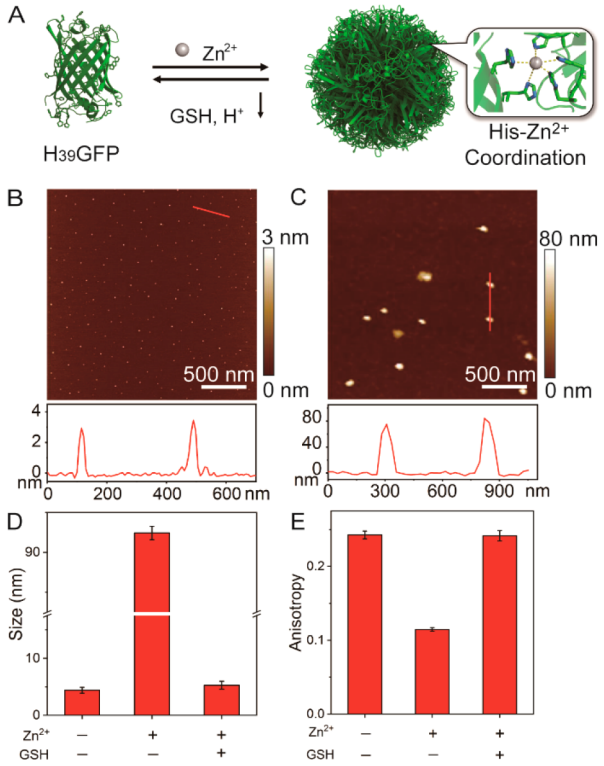

Figure 1. Characterization of the reversible assembly of H_{39}GFP induced by metal ions. (A) Scheme of the H_{39}GFP and metal-ion-induced self-assembly of H_{39}GFP into the nanocomplex. Atomic force microscopy (AFM) images of (B) H_{39}GFP (0.1 μM) and (C) H_{39}GFP/Zn^{2+} (1 μM) complex. Results of (D) hydrodynamic diameters and (E) fluorescence anisotropy of H_{39}GFP (0.1 μM) and H_{39}GFP/Zn^{2+} (1 μM) complex in the absence or presence of GSH (1 mM).

investigated metal ion inducers of the histidine-mediated assembly,[27,28] which was chosen for triggering controllable preassembly of protein cargos. Of particular note, histidine–Zn^{2+} interaction is reversible,[29,30] which is preferable for conditional disassembly and protein release in response to the intracellular microenvironment.

First, the engineered histidine-rich GFP variant, H_{39}GFP, was tested as a self-assembly module. As revealed by atomic force microscopy (AFM; Figure 1B,C), the addition of Zn^{2+} (1 μM) resulted in the H_{39}GFP (0.1 μM) assembly with an average diameter of 80.2 ± 4.6 nm. The hydrodynamic diameter of the H_{39}GFP/Zn^{2+} complex was 92 nm, and the polydispersity index is 0.126 (Figure 1D). Additionally, Zn^{2+}-induced assembly was visualized using confocal laser scanning microscopy (CLSM; Figure S2), and the results indicated the decreased fluorescence anisotropy of H_{39}GFP (Figure 1E). The latter is due to homo-FRET between monomers of H_{39}GFPs in protein assemblies.[31,32] In contrast, eGFP, a control protein without a histidine-rich surface, showed no assembly due to the lack of histidine–Zn^{2+} chelation (Figure S3). Notably, the H_{39}GFP nanocomplex could be reversely disassembled by different conditions, including thiols which have stronger coordination with Zn^{2+} than histidine such as GSH,[33] or lower pH to protonate the imidazole group of histidine.[34] The addition of 1 mM GSH fully restored the hydrodynamic size and fluorescence anisotropy of H_{39}GFP (Figure 1D,E), proving the thiol-triggered nanocomplex disassembly. Moreover, the nanocomplex had good stability in neutral and mild alkaline conditions (pH 7.4/9.0), and partial dissociation was observed when the acidity increased to pH 5.0 (from pH 9.0/7.4 to 5.0, Figure S4). Given the high intracellular thiol concentration (*e.g.*, GSH at the millimole level),[35] and acidic intracellular compartments (pH 5–6),[36] our metal-ion-directed protein assembly could controllably release proteins triggered by intracellular thiols and pH bistimuli.

Preparation and Characterization of Protein@MnO_2 NDs. Manganese ions (Mn^{2+}) can bind to the carboxyl group and thiol group on the surface of the H_{39}GFP to form the Mn–H_{39}GFP complex,[37] where the Mn^{2+} is prone to be oxidized into MnO_2 by oxygen in alkaline solution. The protein nanocomplex was then wrapped into a MnO_2 nanowrapper *via in situ* biomineralization, by mixing Zn^{2+}/H_{39}GFP nanocomplex with manganese chloride ($MnCl_2$) in the buffer solution (Tris-HCl, pH 9.0) at 37 °C for 2 h.[38] In order to maximize protein loading in NDs, we increased the concentration of H_{39}GFP to micromole levels. Meanwhile, the mineralization reaction was as follows: $2Mn^{2+} + 4OH^- + O_2 \rightarrow 2MnO_2 + 2H_2O$, which occurs in mild aqueous media favorable for retaining protein activity. The resulting nanoparticles were further PEGylated with PEG-FA according to the method published (Figure 2A).[39] Transmission electron microscopy (TEM) imaging showed the spheroid shape of the NDs with an average size of 90.3 ± 6.2 nm (Figure 2B, inset). Moreover, after the encapsulation of the Zn^{2+}/H_{39}GFP nanocomplex by MnO_2, the surface ζ potential was switched to −29.5 ± 1.1 mV. The modification by PEG-FA resulted in a decrease in the surface charge to −21.0 ± 1.2 mV (Figure S5). The end product of protein@MnO_2–PEG-FA NDs has a hydrodynamic size of about 100 nm, and the polydispersity index was 0.161 (Figure 2B, inset), which was slightly larger than the diameter measured by TEM. The difference in diameter might be attributed to the coating of the PEG layer. X-ray photoelectron spectroscopy (XPS) spectra were collected for the identification of the surface elements of the NDs. After *in situ* biomineralization, two characteristic peaks of Mn (IV) $2p_{1/2}$ and Mn (IV) $2p_{3/2}$ (654.2 and 642.4 eV) were observed, indicating a successful formation of the MnO_2 nanowrapper. The disappearance of the N 1s peak (400.4 eV) indicated that the inner proteins were completely encapsulated. Further functionalization of NDs by PEG-FA resulted in the reappearance of the N 1s peak and C–O peak in the XPS C 1s spectra, suggesting the successful capping of PEG-FA (Figure 2C, Figure S6 and Table S1).

Protein encapsulation and release of NDs were fluorescently monitored due to the intrinsic fluorescence of H_{39}GFP and its quenchable feature by the MnO_2 nanowrapper. ND encapsulation caused 99% fluorescence quenching of H_{39}GFP, and protein release caused by GSH led to the significant restoration of fluorescence (Figure 2D, Figure S7). Using an electrophoretic mobility shift assay (EMSA), we further validated the protein encapsulation and GSH-induced release of NDs (Figure 2D, inset). The well-retained structure (Figure S8) and fluorescence of H_{39}GFP suggested that the fabrication and disassembly of NDs can be accomplished in a mild condition, which is very important to keep cargo protein functional. Next, we characterized the protein loading efficiency of our ND systems (detailed quantitative methods are shown in Figure S9). The encapsulation efficiency (EE), the portion of the initial proteins

https://dx.doi.org/10.1021/acsnano.9b09024
ACS Nano 2020, 14, 2172–2182

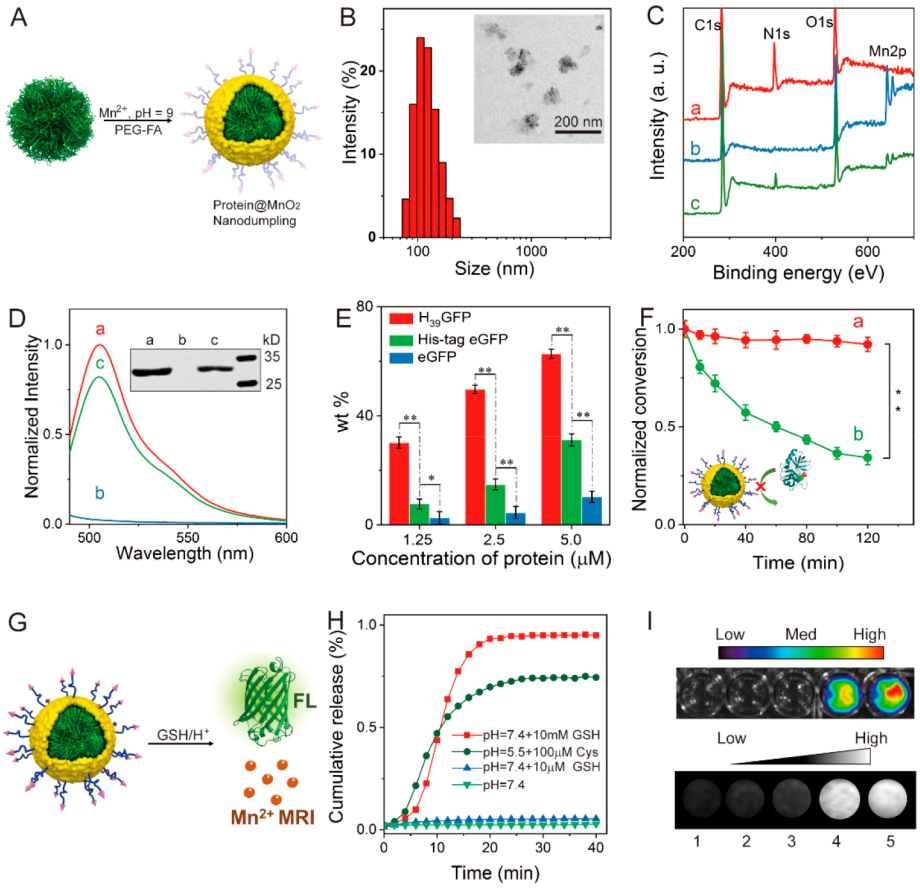

Figure 2. Synthesis and characterization of NDs. (A) Overview of the ND fabrication. (B) Hydrodynamic size of NDs. Inset: TEM observation of NDs. (C) XPS spectra of protein (curve a), and NDs before (curve b) and after (curve c) PEG-FA modification. (D) Fluorescence spectra of H_{39}GFP before encapsulation (curve a), and the NDs (0.1 mg mL^{-1}) in the absence (curve b) and presence of 1 mM GSH (curve c). Inset: SDS-PAGE/in-gel of H_{39}GFP before encapsulation (a), and the NDs in the absence (b) and presence of 1 mM GSH (c). (E) LC of NDs prepared from H_{39}GFP, His-tag eGFP, and eGFP with different concentration. The error bars indicate SD ($n = 3$). * $P < 0.05$, ** $P < 0.01$ (Student's t test). (F) Degradation kinetics of H_{39}GFP (curve a), and NDs (curve b) by trypsin (2 mg mL^{-1}). ** $P < 0.01$ (one-way ANOVA analysis). (G) Scheme of the release of H_{39}GFP and Mn^{2+} from NDs in the presence of GSH and low pH. (H) Time-dependent dynamic releasing profiles of protein from NDs in the presence of GSH and Cys in PBS at different pH (5.5 and 7.4). (I) Fluorescent map (top) and T_1-weighted MR map (bottom) of the NDs dispersed in (1) PBS (pH 5.5); (2) PBS (pH 7.4); (3) PBS (pH 7.4) + GSH (10 μM); (4) PBS (pH 5.5) + Cys (100 μM); and (5) PBS (pH 7.4) + GSH (10 mM).

encapsulated inside nanocarriers, was calculated to be 95%, indicating a super high protein trapping efficiency of the protein preassembly strategy. Another critical parameter is the protein loading capacity (LC), the mass percentage of the nanocarriers occupied by the loaded proteins. Without surface PEG modification, the ratio of H_{39}GFP in the carrier was determined to be about 73 wt %. After the surface coating with PEG, the LC of protein in the total NDs was calculated to be 63 wt % (Figure S10), which is higher than that of most conventional protein nanocarriers (less than 20 wt %).[21] These observations indicate that the ND structure is crucial to efficiently accumulate proteins for high loading. Since the initial amount of Mn^{2+} for biomineralization was consistent, the LC increased with the increasing concentration of proteins (Figure 2E and Table S2). In order to enhance the LC of the NDs, we chose a high concentration of proteins (5.0 μM) in all the following experiments. Moreover, the numbers of proteins (H_{39}GFP) per ND were calculated to be 8077 (see detail in the SI), indicating the high protein LC of the NDs. High protein EE and LC suggest that less protein and nanomaterial mass are needed to achieve a therapeutic dose, which increases the efficiency, economy, and safety of protein delivery.[40]

The stability of NDs was analyzed. The NDs exhibit excellent dispersion stability and no protein leakage after 30 days in cell culture media with serum (10%, v/v) (Figures S11 and S12). Although the free proteins were substantially digested, the inner proteins of NDs showed negligible degradation after 2 h of trypsin treatment (Figure 2F). This result confirmed that the ND efficiently protects protein cargos from enzymatic degradation, which is essential for protein delivery *in vivo*.

The bistimuli-triggered protein release characteristics of NDs were evaluated through biothiol treatment at different pH, which could potentially mimic various physiological conditions (Figure 2G). To assess whether the protein in NDs can be released in a live cell, we tested the protein release from NDs in solutions that mimic the extracellular and intracellular conditions, respectively. As a result, proteins were well maintained in NDs at pH 7.4 or under extracellular fluid-mimicking conditions (pH 7.4 and 10 μM GSH, Figure 2H). A high concentration of GSH (10 mM) that mimics the cytosol reducing environment significantly boosted protein release from NDs, discharging more than 95% at pH 7.4 within 20 min (Figure 2H). A similar release profile (*ca.* 74% in 25 min) was also observed under an endosome/lysosome-like condition at

https://dx.doi.org/10.1021/acsnano.9b09024
ACS Nano 2020, 14, 2172−2182

pH 5.5 and 100 μM cysteine.[41−43] These results imply that NDs enable controllable release of proteins in response to intracellular high concentrations of thiols and acidic intracellular compartments. More importantly, the protein release of NDs can be easily visualized by not only fluorescence but also MRI imaging. GSH-dose-dependent protein release leads to a gradually lightening fluorescence signal (Figure S13), and a synergistically dramatic enhancement of T_1-weighted MRI contrast (Figure 2I). The MRI signal activation is attributed to the following: (1) Manganese, confined in the MnO_2 nanowrapper, is initially inaccessible to the aqueous environment and thus unable to enhance water proton relaxation.[44] (2) Large amounts of Mn^{2+} released by MnO_2 nanowrapper reduction may enhance the protons' transverse and the longitudinal relaxation times, serving as a contrast agent for MRI.[25] (3) The potential contrast is amplified by highly increased relaxivity after binding of Mn^{2+} with proteins,[45] *e.g.*, H_{39}GFP. By surveying the relaxation rates in the presence of increasing concentrations of NDs, the molar relaxivity (effectiveness as a contrast agent) was calculated to be 5.22 mM^{-1} s^{-1}, that is, 31 times over the GSH-treated MnO_2 nanowrapper (0.17 mM^{-1} s^{-1}) (Figure S14). Hence, the fluorescence/MRI bimodal imaging functionality of NDs holds potential for *in situ* probing of protein release *in vivo*. In addition, NDs had negligible effects on the viability of A549 cells, HeLa cells, HCT 116 cells, and MDA-MB-231 cells even at a high dose (up to 500 μg mL^{-1}) (Figure S15), indicating the excellent biocompatibility.

Intracellular Protein Delivery by NDs. The capability of NDs to deliver protein into cells was evaluated by incubating the H_{39}GFP@MnO_2 NDs with HeLa cells in culture media (FBS, 10% v/v). After removing the free NDs by washing, the cells were monitored by live-cell imaging and flow cytometry. After ND treatment, cells exhibited gradually dispersed fluorescence with significantly increasing intensity as observation time extended (up to 4 h), indicating a gradual protein release from internalized NDs (Figure 3A and Figure S16). Furthermore, with the incubation time prolonged, the proteins were homogeneously distributed throughout the cells (Figure S17).

To characterize the endocytic pathways of NDs, we first evaluated the effect of temperature on the cellular uptakes of NDs. As shown in Figure 3B, the protein delivery efficiency decreased dramatically at 4 °C, suggesting that the internalization of NDs is an energy-dependent process.[46] The endocytosis of NDs was further investigated by using different inhibitors for various endocytosis pathways, *i.e.*, amiloride (AMI) for micropinocytosis, methyl-β-cyclodextrin (MCD) for lipid raft-mediated endocytosis, chlorpromazine (CPZ) for the clathrin-mediated endocytosis, and nystatin (NYS) for the caveolin-mediated endocytosis, respectively. Both CPZ and NYS significantly inhibited the cellular uptake of NDs (Figure 3B), indicating that NDs internalize *via* both clathrin- and caveolin-mediated endocytosis.[47,48] Co-localization between H_{39}GFP fluorescence and lysotracker was largely unmatched with an overlapped coefficiency of 26 ± 2% at 6 h after ND treatment, indicating an effective endolysosomal escape of proteins (Figure 3C). This may be attributed to the protonation of multiple histidine residues of H_{39}GFP tagged in acidic endolysosomes, which can cause the "proton sponge effect" for endolysosomal escape.[49]

The potency of NDs for intracellular protein delivery was revealed by 90% GFP-positive cells and 17 times higher cellular fluorescence intensity than free-protein-treated cells (Figure 3D

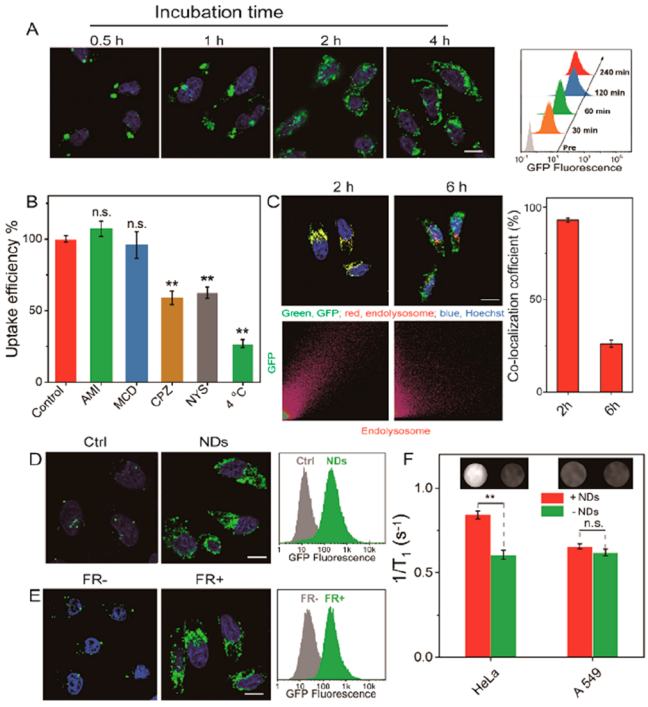

Figure 3. Intracellular protein delivery by NDs. (A) CLSM images and flow-cytometry analysis of HeLa cells treated with NDs at different times. Green, protein; blue, nuclei stained with Hoechst. Scale bar, 20 μm. (B) Relative uptake efficiency of protein uptake by HeLa cells treated with different inhibitors. Data were normalized to those of HeLa cells treated with NDs only (Control). (C) CLSM of HeLa cells after incubation with NDs for 2 and 6 h. Endolysosome was stained with LysoTracker red. Green, H_{39}GFP; red, endolysosome; blue, Hoechst; yellow, colocalization of red and green pixels. Scale bar, 20 μm. (D) CLSM images and flow-cytometry analysis showing cellular uptake of NDs (containing 50 nM) versus protein-free (50 nM) as controls. Scale bar, 20 μm. (E) CLSM images and flow-cytometry analysis of FR+ (HeLa) and FR− (A549) cells incubated with NDs. Scale bar, 20 μm. (F) $1/T_1$ of HeLa cells and A549 cells incubated with NDs for 2 h. Insert: MRI images of HeLa cells and A549 cells incubated with NDs for 2 h. Error bars indicate SD (n = 3). ** P < 0.01 (Student's t test). n.s., not significant.

and Figure S18). Further, compared to the negligible cellular fluorescence in FR-negative cells (A549 cells),[50] FR+ cells, including HeLa, HCT 116, and MDA-MB-231 cells,[51,52] were highly fluorescent (Figure 3E and Figures S19 and S20). The selective delivery of NDs was further confirmed by their self-reported MRI imaging functions. The much higher longitudinal relaxation rate ($1/T_1$) and stronger T_1-weighted MRI contrasts were observed in HeLa cells as compared to that in A549 cells (Figure 3F). In addition, the measurement from inductively coupled plasma optical emission spectrometry (ICP-MS) indicated that the intracellular manganese contents in ND-treated HeLa and A549 cells were 5.7 and 0.31 pg $cell^{-1}$ (Figure S21), respectively, further indicating the targeting-specific delivery of NDs.

Functional Delivery of Therapeutic Proteins. Next, we asked if the NDs could be applied to deliver functional proteins into cells. Ribonuclease A (RNase A), a representative cytotoxic protein, has been evaluated in clinical trials of cancer therapy due to its ability to cleave intracellular RNA and induce cell death.[53,54] We fused RNase A with the assembling tag to generate RNaseA−H_{39}GFP (Figure S22). The corresponding

https://dx.doi.org/10.1021/acsnano.9b09024
ACS Nano 2020, 14, 2172−2182

RNaseA−H_{39}GFP@MnO_2 NDs exhibited a similar size, stability, encapsulation efficiency, and LC to H_{39}GFP@MnO_2 NDs (Figure S23 and Table S3). Moreover, when released from NDs, RNaseA−H_{39}GFP retains its tertiary structures and catalytic activity (Figures S24 and S25).

The intracellular RNase A delivery efficiency of NDs was evaluated and compared with a standard commercial protein delivery kit (Pro-Juice). Flow cytometry revealed that the protein uptake of ND-treated cells is 4.8-fold higher than that of Pro-Juice-treated cells with equal quantities of proteins (Figure 4B). Moreover, Pro-Juice shows nonspecific cellular delivery with relatively low efficiency, whereas NDs exhibit high delivery efficiency in FR+ cells, and a negligible effect in FR− cells (Figure 4C). To investigate the intracellular activity of delivered RNase A, total cellular RNA was extracted for analysis. The total RNA level was reduced by ~60% after ND treatment due to RNase A-catalyzed RNA cleavage, which is significantly higher than that of Pro-Juice-treated cells (30%, Figure 4B). This result was further confirmed by *in situ* cell imaging of total mRNA using a fluorescence *in situ* hybridization (FISH) assay. ND-treated cells exhibited much weaker fluorescence than those treated with free protein and the Pro-Juice method (Figure 4D and Table S4). We further assess the cytotoxicity of delivered RNase A. The NDs dose-dependently inhibited the cell viability of three different FR+ cell lines, however, not affecting the FR− cells, demonstrating the selectivity and cytotoxicity of NDs on target cells (Figure 4E and Figure S26). Similarly, the viability of cells treated with Pro-Juice-delivered proteins and free proteins did not show an obvious difference. Collectively, the NDs could efficiently deliver therapeutic proteins to target cells and exert their intracellular functions, even in the presence of serum.

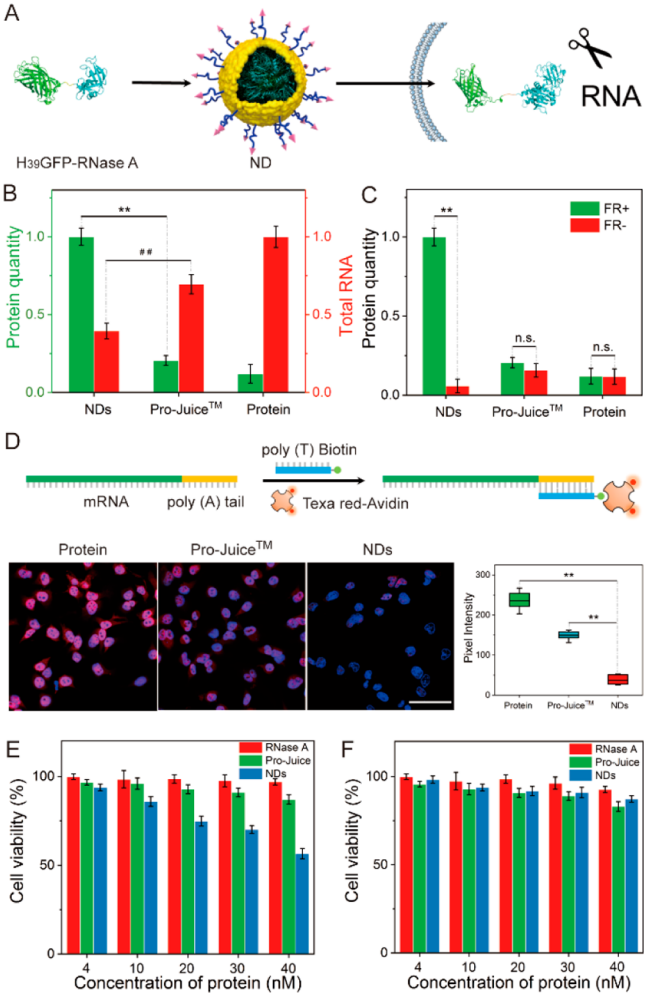

Figure 4. ND-facilitated delivery of functional protein to tumor cells. (A) Overview of synthesis and intracellular delivery of functional RNase A by NDs. (B) Quantitative analysis of protein fluorescence intensity and total RNA to HeLa cells treated with NDs loaded with RNase A. Control experiments were carried out using the protein only and Pro-Juice method. The error bars indicate SD (n = 3). ** P < 0.01 (Student's t test). (C) Quantitative analysis of protein intensity to FR+ (HeLa) cells and FR− (A549) cells. The error bars indicate SD (n = 3). ** P < 0.01 (Student's t test). n.s., not significant. (D) Scheme of the RNase A activity assay using fluorescence *in situ* hybridization (FISH) of cellular mRNA poly(A) tails by poly(T) DNA probes. CLSM observations of HeLa cells preincubated with protein, Pro-Juice, and NDs for 24 h followed by FISH assay to visualize total mRNA. Scale bar, 50 μm. *In vitro* cytotoxicity of RNase A, Pro-Juice, and NDs on (E) FR+ (HeLa) cells and (F) FR− (A549) cells by MTT assay. The error bars indicate SD (n = 3).

***In Vivo* Delivery of Functional Proteins.** *In vivo* protein delivery was investigated to assess the ND system in the therapeutic applications (Figure 5A). Given that HCT116 cells (a FR-positive cell line) were shown to be invasive, highly motile, and highly tumorigenic,[55] the HCT116 cells were selected to set up the tumor xenograft model. In order to track *in vivo* protein delivery, we exploited a near-infrared fluorescent protein (IRFP, Em_{max} = 703 nm) as a model cargo due to its deep tissue penetration (Figure S27).[56] H_{39}GFP−IRFP@MnO_2 NDs also conditionally exhibited a switch-on property of NIR fluorescence (Figure S28). The tumor-targeting delivery of NDs was investigated using mouse xenograft models. Nude mice bearing the HCT 116 tumor were intravenously injected with H_{39}GFP−IRFP@MnO_2 NDs or free proteins, and then monitored by whole-body imaging. As shown in Figure 5B, NDs presented a strong fluorescence signal specifically accumulated at the tumor sites quickly, and it increased over time up to 4 h postinjection, indicating that NDs have a tumor targeting effect and a tumor-selective protein release property. However, the free-protein-treated mouse showed obvious fluorescent signals in most regions without any specificity. Then, *ex vivo* imaging of normal tissues (heart, liver, spleen, lung, and kidneys) and tumor tissue was carried out after the mice were euthanized at 4 h postinjection. At the tumor tissue, the fluorescence intensity of NDs was much stronger than that of the free proteins (Figure 5C). Meantime, to evaluate the *in vivo* biodistribution of NDs, the mice were sacrificed after injection of NDs at different time points, and the Mn^{2+} levels in various organs and the tumor were measured using ICP-MS. As shown in Figure 5D, after 4 h postinjection, the prominent uptake of NDs with ~13.2% injected dose per gram of tissue was observed at the tumor site. The result indicated the high accumulation of NDs at tumor sites. This distribution pattern may be ascribed to the combined effect from both active targeting *via* specific FR-mediated recognition and the enhanced permeability and retention (EPR) effect at the leaky vascular structure around the tumor.[57,58]

Moreover, *in vivo* protein delivery by NDs can be monitored by MRI imaging. The ND-treated mouse exhibited a rapid contrast enhancement in the tumor site as shown in T_1-weighted MRI. The tumor-to-normal (T/N) contrast ratio significantly increased to 127% within 1 h and remained at 167% for 4 h. However, the T/N ratio enhancement was negligible in the free-

https://dx.doi.org/10.1021/acsnano.9b09024
ACS Nano 2020, 14, 2172−2182

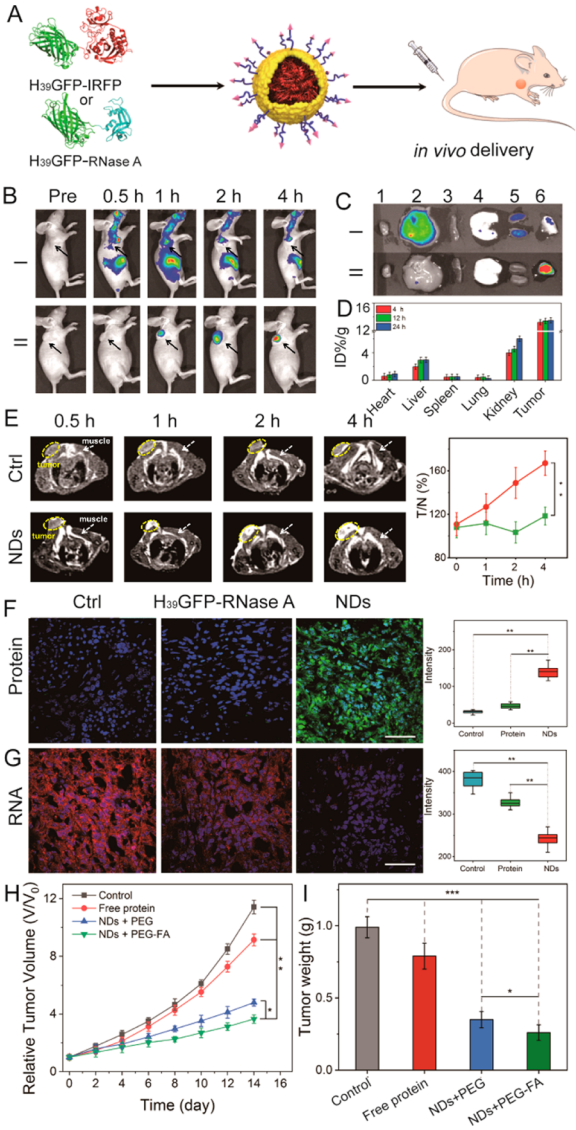

Figure 5. *In vivo* protein delivery of recombinant protein using NDs. (A) Overview of synthesis and *in vivo* delivery of functional protein by NDs. (B) Fluorescence imaging of the free protein (I) and NDs (II). The arrow indicates the tumor area. (C) Fluorescence imaging of the normal and tumor tissues collected from the sacrificed mice at 4 h postinjection of the free protein (I) and NDs (II). (D) Biodistribution of NDs in tumor and normal tissues (1−6: heart, liver, spleen, lung, kidneys, and tumor) determined at different times. (E) T_1-MR images for probing *in vivo* delivery of IRFP in the nude mice bearing a tumor (circled by yellow line) at different times after intravenous injection of protein-free (Ctrl) and NDs. Right panel: quantified T_1-MR signals in skeletal muscle and tumor before and after the injections of the protein-free (green) and NDs (red). ** $P < 0.01$ (one way ANOVA). *In situ* characterization of *in vivo* delivered RNase A by NDs, and the tumor tissue slices were collected from the nude mice bearing a tumor after the different treatments (Ctrl, protein-free, and NDs) and subjected to protein visualization by (F) GFP fluorescent signal and intensity analysis or (G) mRNA visualization by FISH and fluorescence intensity analysis. Scale bar, 100 μm. ** $P < 0.01$ (Student's t test). (H) Tumor growth curves of the HCT116 xenografted mouse model after various treatments indicated. The error bars indicate SD (n = 3). * $P < 0.05$, ** $P < 0.01$ (one way ANOVA). (I) Average tumor weights of different groups. * $P < 0.05$, *** $P < 0.001$ (Student's t test).

protein-treated mouse (Figure 5E). These results confirmed that NDs could be a usable MRI contrast probe for *in situ* probing protein release *in vivo*.

We further utilized the NDs system for functional protein delivery *in vivo*. The nude mice bearing HCT 116 xenografts were injected with RNaseA−H_{39}GFP@MnO_2 NDs or free protein intravenously. The tumors were harvested 24 h postinjection and analyzed. The tumor samples showed obvious GFP fluorescence in the ND-treated mouse, indicating significant amounts of protein accumulation at tumor sites (Figure 5F and Table S5). In contrast, little GFP fluorescence signal was observed in the control group treated with free protein. Moreover, a FISH analysis indicated an approximately 40% degradation of total mRNA in the ND-treated mice, whereas little mRNA signal was lost in the free-protein-treated group (Figure 5G and Table S6). In addition, the β-actin mRNA was quantified by qPCR, confirming the effective and significant degradation of mRNA in the ND-treated mice (Figure S29). These findings further reveal that the ND system can be used as an *in vivo* strategy to delivery functional protein.

The tumor therapeutic efficacy of the NDs was further evaluated *in vivo* by monitoring the tumor volumes during the treatment. Compared with the control group (PBS and free protein), the ND treatment group showed the obvious inhibitory effects on tumor growth (Figure 5H and Figure S30). Particularly, the NDs@PEG-FA group showed the most potent antitumor effect, which is attributed to the FA-mediated cellular uptake. Besides, the tumor masses from all groups were weighted and compared. The data confirmed that the NDs@PEG-FA had the most antitumor potency (Figure 5I), while the body weight of mice had no significant difference in all treated groups (Figure S31). Finally, the histological analysis of major organs (heart, liver, spleen, lung, and kidney) showed no significant off-target damage to normal tissues, indicating low side-effects of the NDs@PEG-FA (Figure S32).

CONCLUSIONS

We reported that a protein@inorganic nanodumpling (ND) structure could function as an efficient vehicle for protein delivery *in vitro* and *in vivo*. In this work, a protein preassembly strategy was developed to fabricate NDs that make use of the metal-ion-mediated assembly of protein cargos with fused histidine-rich assembling tags, followed by *in situ* biomineralization of a MnO_2 nanowrapper. The ND system shows high loading capacity (>63 wt %) and significantly enhanced protein stability, and the protein release is controlled by bistimuli of either an intracellular high thiol concentration or the acidic organelle environment. More importantly, the ND system enables the targeted delivery of functional proteins *in vivo*, which was visualized *via* dual-activatable fluorescence/MRI bimodal imaging. Moreover, the ND system can be engineered to deliver therapeutic protein (*i.e.*, RNase A) to the target tumor cells in a xenografted mouse model, exhibiting excellent therapeutic efficacy. The results suggest that the protein-preassembly-dependent protein@inorganic nanosystem could be adapted to deliver therapeutic proteins efficiently, including natively histidine-rich proteins and natively multicharged proteins. Thus, the ND system provides a promising approach for imaging-guided protein delivery, which holds great potentials for advancing protein drug-facilitated cancer therapeutics.

https://dx.doi.org/10.1021/acsnano.9b09024
ACS Nano 2020, 14, 2172−2182

MATERIALS AND METHODS

Materials. $Zn(NO_3)_2{\cdot}6H_2O$ and $MnCl_2{\cdot}4H_2O$ were obtained from Sinopharm Chemical Reagent Co. Ltd. (Shanghai, China). PEGylation folic acid (PEG_{2000}-FA) was purchased from Ponsure Biological (Shanghai, China). Chlorpromazine (CPZ), nystatin (NYS), amiloride (AMI), and methyl-β-cyclodextrin (MCD) were purchased from MedChem Express. All other chemicals in this study are analytical-grade, and the solutions were prepared with ultrapure water (18.25 MΩ cm).

Recombinant Protein Cloning, Expression, and Purification. The amino acid sequences of H_{39}GFP, RNase A, and IRFP are referred to in previous studies.[59−61] The gene sequences encoding H_{39}GFP, IRFP, and RNase A were codon-optimized and synthesized by Sangon Biotech (Shanghai, China) and then cloned into plasmid pUC57. The IRFP and RNase A were amplified from pUC57-IRFP and pUC57-RNase A, fused with the *H_{39}GFP* gene, and inserted into pET28a to obtain pET28a−H_{39}GFP−IRFP and pET28A−H_{39}GFP−RNase A. The H_{39}GFP was amplified from the pUC57 and was then inserted into *Bam*HI and *Hin*dIII sites of the linearized pET28a plasmid. After the expression plasmids were transformed into *Escherichia coli* BL21 (DE3), a single clone was first cultured overnight in 5 mL liquid LB tubes and then 1% (v/v) inoculated into 3 L of fresh liquid LB. Cells were grown with shaking (250 rpm) at 37 °C. Upon the OD 600 nm reaching 0.8, IPTG was added, and the cell was cultured at 16 °C for ∼16 h before the cell harvesting. The cells were transferred in lysis buffer and ultrasonicated with an ultrasonic cell disintegrator. After centrifuging twice at 4 °C for 30 min, the protein was purified by Ni-NTA (NTA = nitrilotriacetic acid) agarose chromatography (ÄKTA, GE). Fractions containing H_{39}GFP, H_{39}GFP−IRFP, and H_{39}GFP−RNase A proteins were verified by 12% SDS-PAGE. The purified H_{39}GFP, H_{39}GFP−IRFP, and H_{39}GFP−RNase A were quantified by Bradford protein assay with BSA as the standard.

Synthesis of the NDs. For a typical synthesis, 25 μL of Zn^{2+} solution (2 mM) was added in 1 mL of Tris-HCl buffer solution (0.1 M, pH 9.0) containing H_{39}GFP (5 μM) at 25 ± 2 °C. After 30 min, 50 μL of Mn^{2+} solutions (0.1 M) was added under vigorous stirring. After reaction under stirring (300 rpm) at 37 °C for 2 h, the obtained suspension was then dialyzed for 24 h. After that, the protein@MnO_2 was collected by centrifugation. For further PEGylation, 10 mg of protein@MnO_2 was then added into the PEG-FA solution under ultrasound treatment for 2 h. The above steps were repeated 3 times to guarantee efficient PEGylation.[39]

Characterization of the NDs. TEM (acceleration voltage = 200 kV, FEI Tecnai F20) was used to characterize the morphology of NDs. The UV−vis spectra were measured by Cary 60 UV−vis−NIR spectrophotometer (Agilent Technology). Fluorescence spectra were recorded by a QuantaMaster fluorescence spectrophotometer (PTI). The ζ potentials and hydrodynamic diameters were recorded on the Zetasizer Nano-ZS (Malvern Instruments). The amount of Mn was determined using inductively coupled plasma atomic emission spectroscopy (Optima 8000 ICP-MS spectrometer, PerkinElmer). The XPS data were acquired on an ESCALAB 250 photoelectron spectrometer.

Determination of the Encapsulation Efficiency (EE) and Loading Capacity (LC) of the NDs. The ND EE was determined upon the separation of NDs from the preparation medium which contains the unencapsulated protein. The amount of free protein was measured by absorbance by spectrophotometry at 488 nm. The EE of protein was calculated (see detail in the Supporting Information) as

$$\mathrm{EE}\ (\%) = \frac{W_{\text{total-protein}} - W_{\text{supernatant-protein}}}{W_{\text{total-protein}}} \times 100\%$$

To determine protein LC, a 0.1 mg mL^{-1} dispersion of NDs was prepared; 1.0 mL of this dispersion was treated with GSH as a model reducing agent, which leads to complete release of loaded proteins. The amount of loaded protein was determined by Coomassie Brilliant Blue (CBB) assay according to the supplier's protocols. The amount of the Mn in NDs was analyzed by ICP-MS. The EE of protein was calculated (see detail in the Supporting Information) as

$$\mathrm{LC}\ (\%) = \frac{W_{\text{protein}}}{W_{\text{protein}} + W_{\text{MnO}_2} + W_{\text{PEG-FA}}} \times 100\%$$

Release Kinetics in Solution. In the experiment to evaluate release kinetics of H_{39}GFP from NDs, 0.01 mg mL^{-1} NDs were dispersed in PBS (pH 5.5, or pH 7.4) and then incubated with different concentrations of GSH (pH 7.4, 10 mM, or 10 μM) or Cys (pH 5.5, 100 μM). The release kinetics was analyzed by continuously monitoring the fluorescence of released H_{39}GFP.

Cell Culture and Cytotoxicity of NDs. Human cervical cancer cell (HeLa), human breast adenocarcinoma (MDA-MB-231), human colorectal cells (HCT 116), and human lung adenocarcinoma epithelial cells (A549) were cultured in serum-containing culture media (DMEM, 10% v/v FBS) and 1% penicillin/streptomycin containing 5% CO_2 at 37 °C.

The cytotoxicity of NDs was measured using the MTT assay. The cells were seeded in 96-well plates, exposed to the ND solution with different concentrations, and then cultured at 37 °C for 12 or 24 h. After removal of the DMEM media, 20 μL of (5 mg mL^{-1}) MTT reagent was added into the wells and incubated for another 4 h. After that, 80 μL of DMSO was added into the wells, and the absorbance was determined at 570 nm.

Confocal Laser Scanning Microscopy (CLSM) Imaging. Cells were seeded at the glass-bottom plate and incubated for 24 h. After removing the media, 200 μL of NDs (about 50 nM protein) in serum-containing culture media (FBS, 10% v/v) was added into the wells and cultured for 30 min. After removal of the excess NDs, 200 μL of fresh media was added into the wells and incubated for different times (0.5, 1, 2, 4, 12, and 24 h). After washing with PBS, the cells were stained with Hoechst and/or LysoTracker Red. The cells were examined using a CLSM (Nikon). The cells incubated with protein (50 nM protein) were used as controls. The overlap coefficient is quantitatively evaluated by Mander's overlap coefficient (MOC).

Flow Cytometry. The cells were seeded in a 30 mm dish at the density of 3 × 10^5 cells dish^{-1} and then incubated for 24 h. After removing the media, 1 mL of NDs (about 250 nM protein) or free protein (250 nM) in serum-containing culture media was added into the dish and incubated for another 2 h. After washing with PBS, the cells were detached by trypsin. After that, the cells was resuspended in 400 μL of PBS for flow cytometry analysis on a flow cytometer (FACS Calibur, Becton Dickinson).

Determination of Endocytosis Pathways. The cells were seeded in a 24-well plate at the density of 3 × 10^5 cells well^{-1} and then incubated for 24 h. After removing the culture medium, different inhibitors (AMI, 1 mM; MCD, 3 mM; CPZ, 10 μM; NYS, 25 μg mL^{-1}) in 1 mL of fresh culture media were added into the cells and incubated for 1 h. Subsequently, the cells were incubated with NDs at a protein concentration of 200 nM for 2 h. For temperature-dependent experiments, the cells were precultivated at 4 °C for 1 h, followed by treatment with NDs at 200 nM at 4 °C for 2 h. After washing by 4 °C PBS, the cells were lysed with lysis buffer. After centrifugation, the protein concentration was detected using a microplate reader (Infinite M200 PRO, Tecan).

Determination of the Total RNA. The cells were seeded in a dish at 3 × 10^5 cells dish^{-1} (30 mm) and then incubated for 24 h. A 1 mL portion of NDs (about 250 nM protein) or free protein (250 nM) in serum-containing culture media was added into the cells and incubated for 2 h. The cells were washed with PBS and detached with trypsin. Subsequently, the total RNA was extracted by Trizol reagent (Invitrogen).

***In Situ* Visualization of mRNA by Fluorescence *in Situ* Hybridization (FISH).** The cells were seeded in a slide and cultured for 24 h. The cells were washed twice with PBS and incubated with protein, Pro-Juice, and NDs in DMEM (10% FBS, v/v %) at 37 °C for another 24 h. After washing with PBS, the cells were permeabilized with 0.5% Triton X-100. Subsequently, the cells were washed with PBS and rinsed in 2× SSC. Hybridization buffer contained 5 ng μL^{-1} probe, 25% formamide, 1 μg μL^{-1} yeast tRNA, 2× SSC, 10% dextran sulfate. The entire mixture is placed onto one coverslip. The coverslip was inverted onto a slide and sealed with rubber cement. The coverslip was

https://dx.doi.org/10.1021/acsnano.9b09024
ACS Nano 2020, 14, 2172−2182

incubated at 42 °C for 12 h. The coverslips were floated off the slide with 2× SSC, and the cells were washed in 1× SSC and 0.5× SSC for 15 min, respectively. After washing the cells in 4× SSC and 0.1% Triton X-100, the cells were incubated in 4× SSC/1% BSA/2 μg mL^{-1} Texas red-avidin, for 30 min in a humid chamber at 25 °C. The cells were washed by 4× SSC two and 2× SSC for 10 min, respectively. Finally, the cells were washed with PBS and stained with 4′,6-diamidino-2-phenylindole (DAPI).

***In Vivo* Protein Delivery and Imaging Study.** When the tumor reached ∼60 mm^3, the mice were intravenously injected by NDs (containing about 2.6 μg of protein and 1.1 μg of Mn). Fluorescence imaging was taken on a VIS Lumina XR imager under the Cy5.5 filter at different times after injection. MRI was collected on a 3.0 T instrument. The tumors were collected and fixed in 4% paraformaldehyde. Afterward, the frozen tumor slices were sectioned. Protein and mRNA disruptions were visualized by the H_{39}GFP autofluorescence and fluorescence *in situ* hybridization (FISH) of mRNA poly(A) tails by tagged poly(T) DNA probes, respectively. The nuclei were stained with DAPI, and the stained slides were imaged using a CLSM.

***In Vivo* Antitumor Effect of NDs.** When the tumor reached ∼60 mm^3, the mice were randomly allocated into different groups (n = 3). The mice were intravenously injected with (a) PBS (100 μL), (b) free protein (2.0 mg kg^{-1}), (c) NDs@PEG (3.2 mg kg^{-1}), and (d) NDs@PEG-FA (3.2 mg kg^{-1}) every day. The tumor volume and body weight were recorded every 2 days. The tumor volume was calculated as

$$V = \frac{ab^2}{2}$$

where V (mm^3) is the tumor volume, and a (mm) and b (mm) are the larger measured dimension and smaller measured dimension of the tumor, respectively. The relative tumor volume was normalized to their initial sizes (V_0).

Statistical Analysis. Data are presented as mean ± standard deviation (SD) from at least three repeated experiments. The significance of the differences was evaluated using the Student's t test and one way ANOVA. $P < 0.05$ (*) indicate significant and $P < 0.01$ (**) indicate very significant.

ASSOCIATED CONTENT

Supporting Information

The Supporting Information is available free of charge at https://pubs.acs.org/doi/10.1021/acsnano.9b09024.

Description of extensive method and additional data and figures including CLSM images, size distribution histograms, fluorescence anisotropy changes, ζ potential analysis, XPS spectra, normalized fluorescence intensity, CD spectra, UV−vis spectra, SDS-PAGE results, photographs, fluorescence stability, MTT assay results, Mn concentration, enzymatic assay results, cell viability, and H&E staining results (PDF)

AUTHOR INFORMATION

Corresponding Author

Zhou Nie − *State Key Laboratory of Chemo/Biosensing and Chemometrics, College of Chemistry and Chemical Engineering, Hunan Provincial Key Laboratory of Biomacromolecular Chemical Biology, Hunan University, Changsha 410082, P. R. China;* orcid.org/0000-0001-9864-2965; Email: niezhou.hnu@gmail.com

Authors

Xiaohua Zhu − *State Key Laboratory of Chemo/Biosensing and Chemometrics, College of Chemistry and Chemical Engineering, Hunan Provincial Key Laboratory of Biomacromolecular Chemical Biology, Hunan University, Changsha 410082, P. R. China; Key Laboratory of Chemical Biology and Traditional Chinese Medicine Research (Ministry of Education), College of Chemistry and Chemical Engineering, Hunan Normal University, Changsha 410081, P. R. China*

Rui Tang − *State Key Laboratory of Chemo/Biosensing and Chemometrics, College of Chemistry and Chemical Engineering, Hunan Provincial Key Laboratory of Biomacromolecular Chemical Biology, Hunan University, Changsha 410082, P. R. China*

Shigong Wang − *State Key Laboratory of Chemo/Biosensing and Chemometrics, College of Chemistry and Chemical Engineering, Hunan Provincial Key Laboratory of Biomacromolecular Chemical Biology, Hunan University, Changsha 410082, P. R. China*

Xiaoye Chen − *State Key Laboratory of Chemo/Biosensing and Chemometrics, College of Chemistry and Chemical Engineering, Hunan Provincial Key Laboratory of Biomacromolecular Chemical Biology, Hunan University, Changsha 410082, P. R. China*

Jiajun Hu − *College of Biology, Hunan University, Changsha 410082, P. R. China*

Chunyang Lei − *State Key Laboratory of Chemo/Biosensing and Chemometrics, College of Chemistry and Chemical Engineering, Hunan Provincial Key Laboratory of Biomacromolecular Chemical Biology, Hunan University, Changsha 410082, P. R. China;* orcid.org/0000-0002-3078-5553

Yan Huang − *State Key Laboratory of Chemo/Biosensing and Chemometrics, College of Chemistry and Chemical Engineering, Hunan Provincial Key Laboratory of Biomacromolecular Chemical Biology, Hunan University, Changsha 410082, P. R. China;* orcid.org/0000-0001-5965-5739

Honghui Wang − *College of Biology, Hunan University, Changsha 410082, P. R. China;* orcid.org/0000-0002-4420-9733

Shouzhuo Yao − *State Key Laboratory of Chemo/Biosensing and Chemometrics, College of Chemistry and Chemical Engineering, Hunan Provincial Key Laboratory of Biomacromolecular Chemical Biology, Hunan University, Changsha 410082, P. R. China*

Complete contact information is available at: https://pubs.acs.org/10.1021/acsnano.9b09024

Notes

The authors declare no competing financial interest.

ACKNOWLEDGMENTS

This work was financially supported by National Natural Foundation Science of China (21725503, 21675044, 21575038, and 21904039) and the Young Top-notch Talent for Ten Thousand Talent Program.

REFERENCES

(1) Stewart, M. P.; Sharei, A.; Ding, X.; Sahay, G.; Langer, R.; Jensen, K. F. *In Vitro* and *Ex Vivo* Strategies for Intracellular Delivery. *Nature* **2016**, *538*, 183−192.

(2) Gao, X.; Tao, Y.; Lamas, V.; Huang, M.; Yeh, W. H.; Pan, B.; Hu, Y. J.; Hu, J. H.; Thompson, D. B.; Shu, Y.; Li, Y.; Wang, H.; Yang, S.; Xu, Q.; Polley, D. B.; Liberman, M. C.; Kong, W. J.; Holt, J. R.; Chen, Z. Y.; Liu, D. R. Treatment of Autosomal Dominant Hearing Loss by *In Vivo* Delivery of Genome Editing Agents. *Nature* **2018**, *553*, 217−221.

(3) Leader, B.; Baca, Q. J.; Golan, D. E. Protein Therapeutics: A Summary and Pharmacological Classification. *Nat. Rev. Drug Discovery* **2008**, *7*, 21−39.

(4) Akishiba, M.; Takeuchi, T.; Kawaguchi, Y.; Sakamoto, K.; Yu, H. H.; Nakase, I.; Takataninakase, T.; Madani, F.; Gräslund, A.; Futaki, S. Cytosolic Antibody Delivery by Lipid-Sensitive Endosomolytic Peptide. *Nat. Chem.* **2017**, *9*, 751−761.

(5) Mitragotri, S.; Burke, P. A.; Langer, R. Overcoming the Challenges in Administering Biopharmaceuticals: Formulation and Delivery Strategies. *Nat. Rev. Drug Discovery* **2014**, *13*, 655−672.
(6) Cao, L.; Mooney, D. J. Spatiotemporal Control over Growth Factor Signaling for Therapeutic Neovascularization. *Adv. Drug Delivery Rev.* **2007**, *59*, 1340−1350.
(7) Zuris, J. A.; Thompson, D. B.; Shu, Y.; Guilinger, J. P.; Bessen, J. L.; Hu, J. H.; Maeder, M. L.; Joung, J. K.; Chen, Z.-Y.; Liu, D. R. Cationic Lipid-Mediated Delivery of Proteins Enables Efficient Protein-Based Genome Editing *In Vitro* and *In Vivo*. *Nat. Biotechnol.* **2015**, *33*, 73−80.
(8) Fu, J.; Yu, C.; Li, L.; Yao, S. Q. Intracellular Delivery of Functional Proteins and Native Drugs by Cell-Penetrating Poly(Disulfide)s. *J. Am. Chem. Soc.* **2015**, *137*, 12153−12160.
(9) Green, I.; Christison, R.; Voyce, C. J.; Bundell, K. R.; Lindsay, M. A. Protein Transduction Domains: Are They Delivering? *Trends Pharmacol. Sci.* **2003**, *24*, 213−215.
(10) Wang, F.; Chan, C.; Weir, N. R.; Denic, V. The Get1/2 Transmembrane Complex Is an Endoplasmic-Reticulum Membrane Protein Insertase. *Nature* **2014**, *512*, 441−444.
(11) Cronican, J. J.; Thompson, D. B.; Beier, K. T.; McNaughton, B. R.; Cepko, C. L.; Liu, D. R. Potent Delivery of Functional Proteins into Mammalian Cells *In Vitro* and *In Vivo* Using a Supercharged Protein. *ACS Chem. Biol.* **2010**, *5*, 747−752.
(12) Li, M.; Tao, Y.; Shu, Y.; LaRochelle, J. R.; Steinauer, A.; Thompson, D.; Schepartz, A.; Chen, Z. Y.; Liu, D. R. Discovery and Characterization of a Peptide That Enhances Endosomal Escape of Delivered Proteins *In Vitro* and *In Vivo*. *J. Am. Chem. Soc.* **2015**, *137*, 14084−14093.
(13) Wang, M.; Alberti, K.; Sun, S.; Arellano, C. L.; Xu, Q. Combinatorially Designed Lipid-Like Nanoparticles for Intracellular Delivery of Cytotoxic Protein for Cancer Therapy. *Angew. Chem.* **2014**, *126*, 2937−2942.
(14) Wang, M.; Zuris, J. A.; Meng, F.; Rees, H.; Sun, S.; Deng, P.; Han, Y.; Gao, X.; Pouli, D.; Wu, Q.; Georgakoudi, I.; Liu, D. R.; Xu, Q. Efficient Delivery of Genome-Editing Proteins Using Bioreducible Lipid Nanoparticles. *Proc. Natl. Acad. Sci. U. S. A.* **2016**, *113*, 2868−2873.
(15) Postupalenko, V.; Desplancq, D.; Orlov, I.; Arntz, Y.; Spehner, D.; Mely, Y.; Klaholz, B. P.; Schultz, P.; Weiss, E.; Zuber, G. Protein Delivery System Containing a Nickel-Immobilized Polymer for Multimerization of Affinity-Purified His-Tagged Proteins Enhances Cytosolic Transfer. *Angew. Chem., Int. Ed.* **2015**, *54*, 10583−10586.
(16) Kamaly, N.; Fredman, G.; Subramanian, M.; Gadde, S.; Pesic, A.; Cheung, L.; Fayad, Z. A.; Langer, R.; Tabas, I.; Farokhzad, O. C. Development and *In Vivo* Efficacy of Targeted Polymeric Inflammation-Resolving Nanoparticles. *Proc. Natl. Acad. Sci. U. S. A.* **2013**, *110*, 6506−6511.
(17) Zhao, M.; Liu, Y.; Hsieh, R. S.; Wang, N.; Tai, W.; Joo, K.-I.; Wang, P.; Gu, Z.; Tang, Y. Clickable Protein Nanocapsules for Targeted Delivery of Recombinant p53 Protein. *J. Am. Chem. Soc.* **2014**, *136*, 15319−15325.
(18) Dutta, K.; Hu, D.; Zhao, B.; Ribbe, A. E.; Zhuang, J.; Thayumanavan, S. Templated Self-Assembly of a Covalent Polymer Network for Intracellular Protein Delivery and Traceless Release. *J. Am. Chem. Soc.* **2017**, *139*, 5676−5679.
(19) Tang, R.; Kim, C. S.; Solfiell, D. J.; Rana, S.; Mout, R.; Velázquez-Delgado, E. M.; Chompoosor, A.; Jeong, Y.; Yan, B.; Zhu, Z.-J.; Kim, C.; Hardy, J. A.; Rotello, V. M. Direct Delivery of Functional Proteins and Enzymes to the Cytosol Using Nanoparticle-Stabilized Nanocapsules. *ACS Nano* **2013**, *7*, 6667−6673.
(20) Mout, R.; Ray, M.; Tay, T.; Sasaki, K.; Tonga, G. Y.; Rotello, V. M. General Strategy for Direct Cytosolic Protein Delivery *via* Protein-Nanoparticle Co-Engineering. *ACS Nano* **2017**, *11*, 6416−6421.
(21) Wu, J.; Kamaly, N.; Shi, J.; Zhao, L.; Xiao, Z.; Hollett, G.; John, R.; Ray, S.; Xu, X.; Zhang, X.; Kantoff, P. W.; Farokhzad, O. C. Development of Multinuclear Polymeric Nanoparticles as Robust Protein Nanocarriers. *Angew. Chem., Int. Ed.* **2014**, *53*, 8975−8979.
(22) Prasetyanto, E. A.; Bertucci, A.; Septiadi, D.; Corradini, R.; Castrohartmann, P.; Cola, L. D. Breakable Hybrid Organosilica Nanocapsules for Protein Delivery. *Angew. Chem., Int. Ed.* **2016**, *55*, 3323−3327.
(23) Fan, H.; Zhao, Z.; Yan, G.; Zhang, X.; Yang, C.; Meng, H.; Chen, Z.; Liu, H.; Tan, W. A Smart DNAzyme-MnO_2 Nanosystem for Efficient Gene Silencing. *Angew. Chem., Int. Ed.* **2015**, *54*, 4801−4805.
(24) Zhu, W.; Dong, Z.; Fu, T.; Liu, J.; Chen, Q.; Li, Y.; Zhu, R.; Xu, L.; Liu, Z. Modulation of Hypoxia in Solid Tumor Microenvironment with MnO_2 Nanoparticles to Enhance Photodynamic Therapy. *Adv. Funct. Mater.* **2016**, *26*, 5490−5498.
(25) Deng, R.; Xie, X.; Vendrell, M.; Chang, Y.-T.; Liu, X. Intracellular Glutathione Detection Using MnO_2-Nanosheet-Modified Upconversion Nanoparticles. *J. Am. Chem. Soc.* **2011**, *133*, 20168−20171.
(26) Zhao, Z.; Fan, H.; Zhou, G.; Bai, H.; Liang, H.; Wang, R.; Zhang, X.; Tan, W. Activatable Fluorescence/MRI Bimodal Platform for Tumor Cell Imaging *via* MnO_2 Nanosheet-Aptamer Nanoprobe. *J. Am. Chem. Soc.* **2014**, *136*, 11220−11223.
(27) Luo, Q.; Hou, C.; Bai, Y.; Wan, R.; Liu, J. Protein Assembly: Versatile Approaches to Construct Highly Ordered Nanostructures. *Chem. Rev.* **2016**, *116*, 13571−13632.
(28) Sontz, P. A.; Bailey, J. B.; Ahn, S.; Tezcan, F. A. A Metal Organic Framework with Spherical Protein Nodes: Rational Chemical Design of 3D Protein Crystals. *J. Am. Chem. Soc.* **2015**, *137*, 11598−11601.
(29) Schmidt, S.; Reinecke, A.; Wojcik, F.; Pussak, D.; Hartmann, L.; Harrington, M. J. Metal-Mediated Molecular Self-Healing in Histidine-Rich Mussel Peptides. *Biomacromolecules* **2014**, *15*, 1644−1652.
(30) Eibling, M. J.; MacDermaid, C. M.; Qian, Z.; Lanci, C. J.; Park, S.-J.; Saven, J. G. Controlling Association and Separation of Gold Nanoparticles with Computationally Designed Zinc-Coordinating Proteins. *J. Am. Chem. Soc.* **2017**, *139*, 17811−17823.
(31) Chan, F. T. S.; Kaminski, C. F.; Schierle, G. S. K. HomoFRET Fluorescence Anisotropy Imaging as a Tool to Study Molecular Self-Assembly in Live Cells. *ChemPhysChem* **2011**, *12*, 500−509.
(32) Lei, C.; Huang, Y.; Nie, Z.; Hu, J.; Li, L.; Lu, G.; Han, Y.; Yao, S. A Supercharged Fluorescent Protein as a Versatile Probe for Homogeneous DNA Detection and Methylation Analysis. *Angew. Chem., Int. Ed.* **2014**, *53*, 8358−8362.
(33) Dudev, T.; Lim, C. Principles Governing Mg, Ca, and Zn Binding and Selectivity in Proteins. *Chem. Rev.* **2003**, *103*, 773−787.
(34) Ling, D.; Park, W.; Park, S. J.; Lu, Y.; Kim, K. S.; Hackett, M. J.; Kim, B. H.; Yim, H.; Jeon, Y. S.; Na, K.; Hyeon, T. Multifunctional Tumor pH-Sensitive Self-Assembled Nanoparticles for Bimodal Imaging and Treatment of Resistant Heterogeneous Tumors. *J. Am. Chem. Soc.* **2014**, *136*, 5647−5655.
(35) Yang, G.; Xu, L.; Chao, Y.; Xu, J.; Sun, X.; Wu, Y.; Peng, R.; Liu, Z. Hollow MnO_2 as a Tumor-Microenvironment-Responsive Biodegradable Nano-Platform for Combination Therapy Favoring Antitumor Immune Responses. *Nat. Commun.* **2017**, *8*, 902.
(36) Zhao, X.; Yang, C. X.; Chen, L. G.; Yan, X. P. Dual-Stimuli Responsive and Reversibly Activatable Theranostic Nanoprobe for Precision Tumor-Targeting and Fluorescence-Guided Photothermal Therapy. *Nat. Commun.* **2017**, *8*, 14998.
(37) Yang, T.; Wang, Y.; Ke, H.; Wang, Q.; Lv, X.; Wu, H.; Tang, Y.; Yang, X.; Chen, C.; Zhao, Y.; Chen, H. Protein-Nanoreactor-Assisted Synthesis of Semiconductor Nanocrystals for Efficient Cancer Theranostics. *Adv. Mater.* **2016**, *28*, 5923−5930.
(38) Chen, Q.; Feng, L.; Liu, J.; Zhu, W.; Dong, Z.; Wu, Y.; Liu, Z. Intelligent Albumin-MnO_2 Nanoparticles as pH-/H_2O_2-Responsive Dissociable Nanocarriers to Modulate Tumor Hypoxia for Effective Combination Therapy. *Adv. Mater.* **2016**, *28*, 7129−7136.
(39) Chen, Y.; Ye, D.; Wu, M.; Chen, H.; Zhang, L.; Shi, J.; Wang, L. Break-Up of Two-Dimensional MnO_2 Nanosheets Promotes Ultrasensitive pH-Triggered Theranostics of Cancer. *Adv. Mater.* **2014**, *26*, 7019−7026.
(40) Yu, M.; Wu, J.; Shi, J.; Farokhzad, O. C. Nanotechnology for Protein Delivery: Overview and Perspectives. *J. Controlled Release* **2016**, *240*, 24−37.
(41) Arunachalam, B.; Phan, U. T.; Geuze, H. J.; Cresswell, P. Enzymatic Reduction of Disulfide Bonds in Lysosomes: Character-

https://dx.doi.org/10.1021/acsnano.9b09024
ACS Nano 2020, 14, 2172−2182

ization of A Gamma-Interferon-Inducible Lysosomal Thiol Reductase (GILT). *Proc. Natl. Acad. Sci. U. S. A.* **2000**, *97*, 745−750.
(42) Myhre, O.; Andersen, J. M.; Aarnes, H.; Frode, F. Evaluation of the Probes 2′, 7′-Dichlorofluorescin Diacetate, Luminol, and Lucigenin as Indicators of Reactive Species Formation. *Biochem. Pharmacol.* **2003**, *65*, 1575−1582.
(43) Baird, S. K.; Kurz, T.; Brunk, U. T. Metallothionein Protects against Oxidative Stress-Induced Lysosomal Destabilization. *Biochem. J.* **2006**, *394*, 275−283.
(44) Fan, H.; Yan, G.; Zhao, Z.; Hu, X.; Zhang, W.; Liu, H.; Fu, X.; Fu, T.; Zhang, X. B.; Tan, W. A Smart Photosensitizer-Manganese Dioxide Nanosystem for Enhanced Photodynamic Therapy by Reducing Glutathione Levels in Cancer Cells. *Angew. Chem., Int. Ed.* **2016**, *55*, 5477−5482.
(45) Mi, P.; Kokuryo, D.; Cabral, H.; Wu, H.; Terada, Y.; Saga, T.; Aoki, I.; Nishiyama, N.; Kataoka, K. A pH-Activatable Nanoparticle with Signal-Amplification Capabilities for Non-Invasive Imaging of Tumour Malignancy. *Nat. Nanotechnol.* **2016**, *11*, 724−730.
(46) Wang, C.; Xu, H.; Liang, C.; Liu, Y.; Li, Z.; Yang, G.; Cheng, L.; Li, Y.; Liu, Z. Iron Oxide@Polypyrrole Nanoparticles as a Multifunctional Drug Carrier for Remotely Controlled Cancer Therapy with Synergistic Antitumor Effect. *ACS Nano* **2013**, *7*, 6782−6795.
(47) Sun, W.; Jiang, T.; Lu, Y.; Reiff, M.; Mo, R.; Gu, Z. Cocoon-Like Self-Degradable DNA Nanoclew for Anticancer Drug Delivery. *J. Am. Chem. Soc.* **2014**, *136*, 14722−14725.
(48) Sun, W.; Ji, W.; Hall, J. M.; Hu, Q.; Wang, C.; Beisel, C. L.; Gu, Z. Self-Assembled DNA Nanoclews for the Efficient Delivery of CRISPR-Cas9 for Genome Editing. *Angew. Chem., Int. Ed.* **2015**, *54*, 12029−12033.
(49) Zhang, X.; Chen, D.; Ba, S.; Zhu, J.; Zhang, J.; Hong, W.; Zhao, X.; Hu, H.; Qiao, M. Poly(L-Histidine) Based Triblock Copolymers: pH Induced Reassembly of Copolymer Micelles and Mechanism Underlying Endolysosomal Escape for Intracellular Delivery. *Biomacromolecules* **2014**, *15*, 4032−4025.
(50) Jiang, Q.-Y.; Lai, L.-H.; Shen, J.; Wang, Q.-Q.; Xu, F.-J.; Tang, G.-P. Gene Delivery to Tumor Cells by Cationic Polymeric Nanovectors Coupled to Folic Acid and the Cell-Penetrating Peptide Octaarginine. *Biomaterials* **2011**, *32*, 7253−7262.
(51) He, M.; Ro, L.; Liu, J.; Chu, C.-C. Folate-Decorated Arginine-Based Poly (Ester Urea Urethane) Nanoparticles as Carriers for Gambogic Acid and Effect on Cancer Cells. *J. Biomed. Mater. Res., Part A* **2017**, *105*, 475−490.
(52) Cui, S.; Yin, D.; Chen, Y.; Di, Y.; Chen, H.; Ma, Y.; Achilefu, S.; Gu, Y. *In Vivo* Targeted Deep-Tissue Photodynamic Therapy Based on Near-Infrared Light Triggered Upconversion Nanoconstruct. *ACS Nano* **2013**, *7*, 676−688.
(53) Lee, J. E.; Raines, R. T. Ribonucleases as Novel Chemotherapeutics. *BioDrugs* **2008**, *22*, 53−58.
(54) Liu, M.; Shen, S.; Wen, D.; Li, M.; Li, T.; Chen, X.; Gu, Z.; Mo, R. Hierarchical Nanoassemblies-Assisted Combinational Delivery of Cytotoxic Protein and Antibiotic for Cancer Treatment. *Nano Lett.* **2018**, *18*, 2294−2303.
(55) Saldanha, R. G.; Xu, N.; Molloy, M. P.; Veal, D. A.; Baker, M. S. Differential Proteome Expression Associated with Urokinase Plasminogen Activator Receptor (uPAR) Suppression in Malignant Epithelial Cancer. *J. Proteome Res.* **2008**, *7*, 4792−4806.
(56) Feng, G.; Luo, C.; Yi, H.; Yuan, L.; Lin, B.; Luo, X.; Hu, X.; Wang, H.; Lei, C.; Nie, Z.; Yao, S. DNA Mimics of Red Fluorescent Proteins (RFP) Based on G-Quadruplex-Confined Synthetic RFP Chromophores. *Nucleic Acids Res.* **2017**, *45*, 10380−10392.
(57) Zhao, R.; Wang, B.; Yang, X.; Xiao, Y.; Wang, X.; Shao, C.; Tang, R. A Drug-Free Tumor Therapy Strategy: Cancer-Cell-Targeting Calcification. *Angew. Chem., Int. Ed.* **2016**, *55*, 5225−5229.
(58) Sowers, M. A.; McCombs, J. R.; Wang, Y.; Paletta, J. T.; Morton, S. W.; Dreaden, E. C.; Boska, M. D.; Ottaviani, M. F.; Hammond, P. T.; Rajca, A.; Johnson, J. A. Redox-Responsive Branched-Bottlebrush Polymers for *In Vivo* MRI and Fluorescence Imaging. *Nat. Commun.* **2014**, *5*, 5460.
(59) Thompson, D. B.; Cronican, J. J.; Liu, D. R. Engineering and Identifying Supercharged Proteins for Macromolecule Delivery into Mammalian Cells. *Methods Enzymol.* **2012**, *503*, 293−319.
(60) Yu, D.; Baird, M. A.; Allen, J. R.; Howe, E. S.; Klassen, M. P.; Reade, A.; Makhijani, K.; Song, Y.; Liu, S.; Murthy, Z.; Zhang, S. Q.; Weiner, O. D.; Kornberg, T. B.; Jan, Y. N.; Davidson, M. W.; Shu, X. A Naturally Monomeric Infrared Fluorescent Protein for Protein Labeling *In Vivo*. *Nat. Methods* **2015**, *12*, 763−765.
(61) Nambiar, K. P.; Stackhouse, J.; Presnell, S. R.; Benner, S. A. Expression of Bovine Pancreatic Ribonuclease A in Escherichia Coli. *Eur. J. Biochem.* **1987**, *163*, 67−71.

https://dx.doi.org/10.1021/acsnano.9b09024
ACS Nano 2020, 14, 2172−2182